

Contents lists available at ScienceDirect

Chemical Engineering Journal

journal homepage: www.elsevier.com/locate/cej





Supramolecular amino acid-based metallo-nanozyme through multicomponent coordination self-assembly for in-site tumor synergistic catalytic-chemotherapy

Shuo Zhang ^a, Yongxin Li ^{a,*}, Chunlei Liu ^a, Yanhui Zhang ^a, Pan Sun ^{b,*}, Xiaopeng Lan ^{a,*}, Chunzhao Liu ^{a,*}

ARTICLE INFO

Keywords: Coordination self-assembly Amino acid Metallo-nanozyme Catalytic therapy Chemotherapy

ABSTRACT

Simple biomolecules-based supramolecular self-assembly hold great promise on the fabrication of nanozyme for mimicking natural enzyme, both structurally and functionally. However, it remains a formidable challenge to design of tumor-specific nanozyme with promoted therapeutic efficiencies starting from such small biological molecule combinations and their cooperative interactions. Inspired by the metalloenzyme in living systems, i.e., peroxidase, herein the construction of metallo-nanozyme through a facile multicomponent coordination selfassembly based on the combination of amino acid, chemotherapeutic motif and metal ions is reported. The resulting metallo-nanozyme possess uniform size distribution, well-defined spherical nanostructure and high chemical drugs contents. Most importantly, the metallo-nanozyme depletes specifically high-level glutathione (GSH) in tumor cell and converts Fe³⁺ to Fe²⁺ for subsequent transformation of overproduced hydrogen peroxide (H₂O₂) into highly cytotoxic hydroxyl radical (·OH) in peroxidase-like catalytic manner. Meanwhile, the metallonanozyme are also activated in situ to release the chemical drugs in tumor cell for enhanced chemotherapy. In vitro and in vivo evaluations demonstrate that the supramolecular metallo-nanozyme suppresses remarkably tumor growth via combined catalytic-chemotherapy and without any systemic toxicity. Therefore, this study demonstrates that the tumor-specific biomimetic nanozyme with advanced catalytic therapeutic efficacy could be achieved through cooperative coordination of small biomolecules or therapeutic drugs, opening up opportunities in the development of catalytic anticancer nanozyme for efficiently combat cancers.

1. Introduction

Chemotherapy remains mainstay of treatment in most cancer cases because of its high efficiency [1], and various chemotherapeutic drugs, including doxorubicin, 5-fluorouracil, paclitaxel, irinotecan, and cisplatin, have gained great success in clinics [2]. Unfortunately, these chemotherapeutic agents often caused severe adverse effects and easily acquired multidrug resistance, which are exactly major limitations of conventional chemotherapy towards conquering cancer [3]. Although the past few decades have witnessed the robust development of numerous nanomedicines aiming to prolonged blood circulation and tumor-specific delivery, the majority of the nanodrugs clinically do not show any promoted therapeutic performance [4]. Recently, catalytic

nanoarchitectures with intrinsic biological activities that could respond uniquely to tumor microenvironment, held a new era for cancer nanomedicine [5]. With the specific stimuli in tumor microenvironment, i.e., overproduced H_2O_2 , high level of glucose, over-expressed glutathione (GSH), the nanocatalysts regulated the intratumoral biochemical reaction, resulting in explosive production of reactive oxygen species (ROS), exhaustion of energy metabolism, and depletion of antioxidants, thereby endowing satisfactory antitumor efficacy [6]. To date, a variety of nanomaterials with natural enzyme-mimicking activity have been discovered and extensively used in cancer therapy [7]. Moreover, the nanozymes that integrate the functions of both nature enzymes and nanomaterials exhibit unque advantages, such as low cost, superior stability against harsh conditions and tunable catalytic activities [8]. For

E-mail addresses: liyx@qdu.edu.cn (Y. Li), sunp@uchicago.edu (P. Sun), alanhenry@126.com (X. Lan), czliu@qdu.edu.cn (C. Liu).

^a State Key Laboratory of Bio-fibers and Eco-textiles, Institute of Biochemical Engineering, The Affiliated Qingdao Central Hospital of Qingdao University, College of Materials Science and Engineering, Qingdao University, Qingdao 266071, China

b NSF's ChemMatCARS, University of Chicago, Chicago, IL 60637, USA

^{*} Corresponding authors.

example, PtCo nanoparticles as oxidase mimics were used to catalyze the oxidation reaction for inducing cellular oxidative damage towards antitumor therapy [9]. Nitrogen-doped carbon nanomaterials exhibited oxidase-and peroxidase-like catalytic activity are reported to generate ROS for tumor suppression [10]. In spite of the therapeutic potential of nanozyme, most of the reported nanozymes, only from functional viewpoint, fabricated by inorganic materials, which inevitably suffered from high toxicity and serious inflammation [7,11]. In this regard, supramolecular biomolecule-based nanomaterials have attracted considerable attention for constructing nanozymes, especially amino acids or peptides [12], which serve as the primary unit of natural enzymes. The nanozymes can be rationally designed through self-assembly of key amino acids and cofactors that involve in forming catalytic active center. Yan et al., [13] reported the nanozymes with photooxidase-mimicking activity based on amphiphilic amino acid and photosensitizers coassembly, exhibiting superior photocatalytic activity. In our previous work, we also employed amphiphilic amino acids as building blocks for construction of catalase-like photosensitizing nanozyme with the assistance of metal ions, ameliorating the intratumoral hypoxic condition for promoted the photodynamic activity [14]. However, these nanozyme generally show catalytic performances with external light activation, which restricting their catalytic activities as artificial nanozyme. Very recently, Li et al., [15] demonstrated that copper ions (Cu²⁺) could act as building blocks for construction of nanosized oxidative stress amplifier, which significantly sensitized immunotherapy by virtue of its GSH oxidase-like activity, but the nanozyme itself possessed little anticancer effect. Thus, the selection of small biomolecule combination and the precise control of their cooperative interaction to realize high specificity and therapeutic efficiency without the need of external energy input is still challenging in the design of catalytic anticancer nanozyme.

A large number of enzymes in nature are metalloenzymes, i.e., peroxidase, which integrate all of metal ions, organic cofactors and amino acid resides through cooperative coordination interactions [16]. The ferric clusters as the catalytic active center of the redox reactions via the valence shift between the two states (Fe³⁺ and Fe²⁺) [17]. Many of chemotherapeutic agents contain metal ion-binding group (i.e., amidogen, oxhydryl). In light of this, from both of functional and structural perspective, we proposed herein a multicomponent coordination selfassembly strategy based on the combination of amino acid, chemotherapeutic drug and metal ions to design and engineer biomimetic metalloenzyme for catalytic-chemotherapy. Notably, the chemotherapeutic agent served as both of structural cofactors and therapeutic drugs. Moreover, modulating ROS have been found to enhance the therapeutic effect of chemical drugs by overcoming the multidrug resistance in cancer [18], the catalytic therapy based on generation of ROS was also powerful companion for chemotherapy.

Spherical nanostructures are readily obtained by Fe ion-coordinated multicomponent self-assembly of the metal-binding amino acid and a representative chemotherapeutic drug, doxorubicin (DOX) (Fig. 1). Upon internalization into cancer cells, the valence state shift from ${\rm Fe}^{3+}$ to ${\rm Fe}^{2+}$ of the resulting multicomponent assemblies occurred by reduction of high-level GSH, accompanied by oxidation of GSH to GSSG. Then ${\rm Fe}^{2+}$ reacted with overproduced endogenous ${\rm H_2O_2}$ to generate highly toxic ·OH through Fenton-type Harber-Weiss, thus leading to peroxidase-mimicking activities of the metallo-nanozyme. The DOX was further specifically released in response to tumor tissue for the enhanced chemotherapy through ROS-mediated signaling. In this way, an augmentative synergistic efficacy of chemo-catalytic therapy could be achieved by the peroxidase-like metallo-nanozyme, which would effectively suppress cancer growth in a more efficient and biosafe manner.

2. Results and discussion

Fmoc-S (fluorenylmethoxycarbonyl-L-Serine) was selected as the model amino acid for coordination self-assembly due to its strong metalbinding ability and superior self-assembly features. By mixing simply a solution of ferric chloride (FeCl₃) and a solution of Fmoc-S in dimethylsulfoxide (DMSO), an opalescent and turbid colloid suspension with size of approximately 104 nm was obtained (Fig. 2a), labeled as Fmoc-S/ Fe. Scanning electron microscopy (SEM) image (Figure S1) and transmission electron microscopy (TEM) image (Fig. 2b) revealed that the Fmoc-S/Fe are spherical, solid nanoparticles with uniform size distributions on ca. 100 nm, which are consistent with DLS result. As a comparison, Fmoc-S would lead to massive precipitation in the absence of Fe³⁺ ions. Subsequently, we investigated the mechanism of selfassembly of Fmoc-S triggered by Fe³⁺. The infrared (IR) spectrum of Fmoc-S/Fe was measured and compared with that of Fmoc-S (Fig. 2c). The distinct bands at 1620 cm⁻¹ and 1387 cm⁻¹ in the spectrum of Fmoc-S/Fe corresponding to asymmetric and symmetric stretching vibrations appeared, indicated that the carboxyl groups of Fmoc-S were coordinated to the Fe³⁺ [19]. The C-OH stretching peak at 1200 cm⁻¹ and the O-H bending peak at 988 cm⁻¹ were apparently disappeared, indicating that iron ions were also combined with the hydroxyl of Fmoc-S [20]. The molar ratio of Fmoc-S/Fe³⁺ obtained from quantitative component analysis are close to 3:1. These results indicated that the formation of nanoparticles was driven by the complexation of Fe³⁺ with the carboxyl and hydroxyl groups of Fmoc-S. A molecular dynamics (MD) simulation was carried out to further provide the evidence on coordination self-assembly, the simulation results showed that each ferric coordination sphere involved two Fmoc-S molecules, each Fmoc-S molecule offered a hydroxyl group and a carboxyl group for

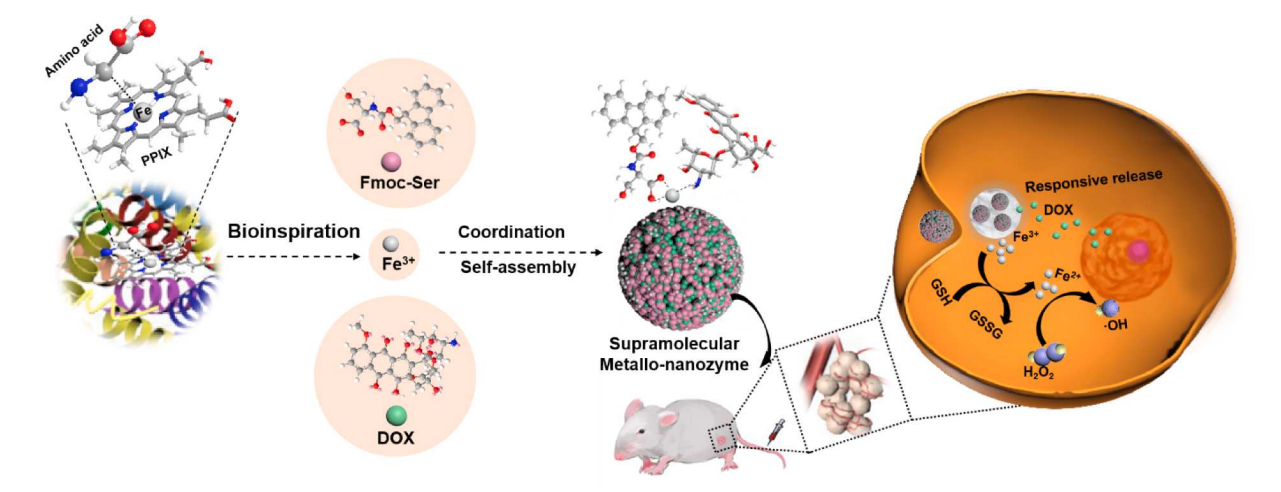


Fig. 1. Schematic illustration for the construction of supramolecular metallo-nanozyme for tumor-specific catalytic-chemotherapy.

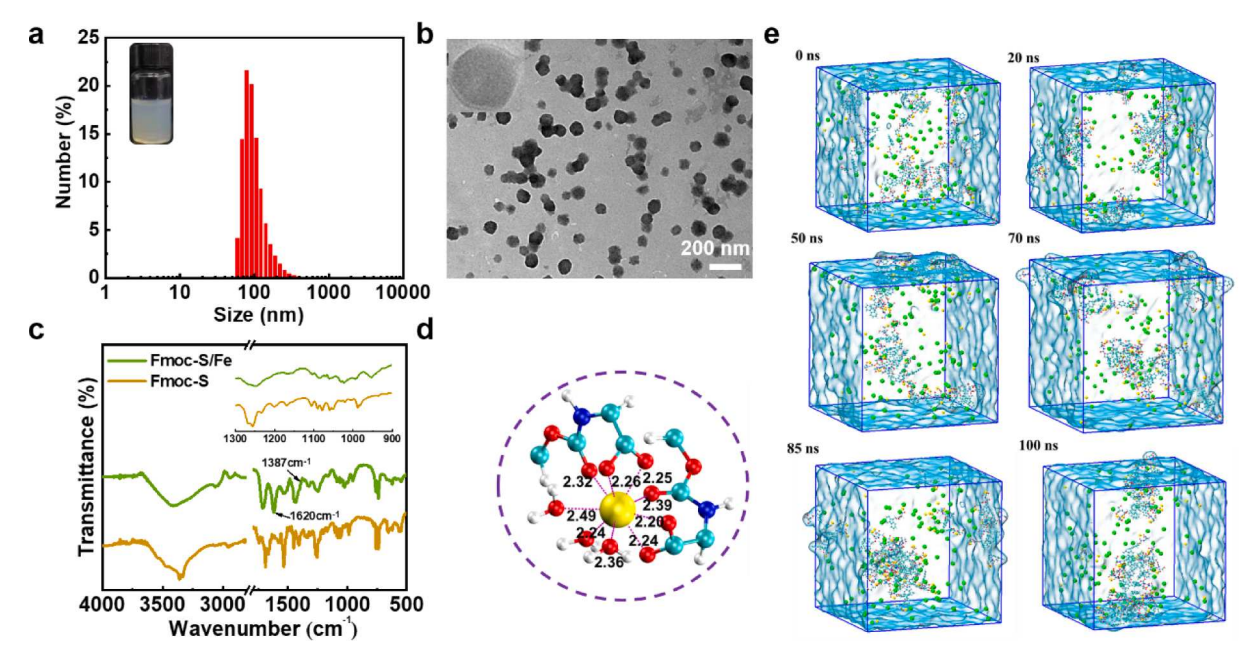


Fig. 2. Morphology, FTIR spectra, coordination pattern and evolution of Fmoc-S/Fe nanoparticles. a) DLS profile with picture of the sample shown in the inset. b) TEM image. c) FTIR spectra. d) Proposed spatial coordination conformation of Fmoc-S and Fe³⁺, as well as the lengths of the coordination bonds. e) Snapshots of simulation box at different simulation time. The Fmoc-S is represented as cyan, red and white spheres, Fe³⁺ is represented as yellow sphere, solvent water is represented as a transparent box. The unit of bond length labeled in the figure is angstrom.

coordination (Fig. 2d). In recent work, we demonstrated Fmoc-Cys could form hollow nanovesicles in the presence of Fe^{3+} ions [14]. The soild or hollow state of these nanoparticles was probably attributed to

the different coordination modes and stoichiometry, which further influcence self-organization process of molecular subunits. The assembly of Fmoc-Cys/Fe nanovesicle undergo the formation of droplets

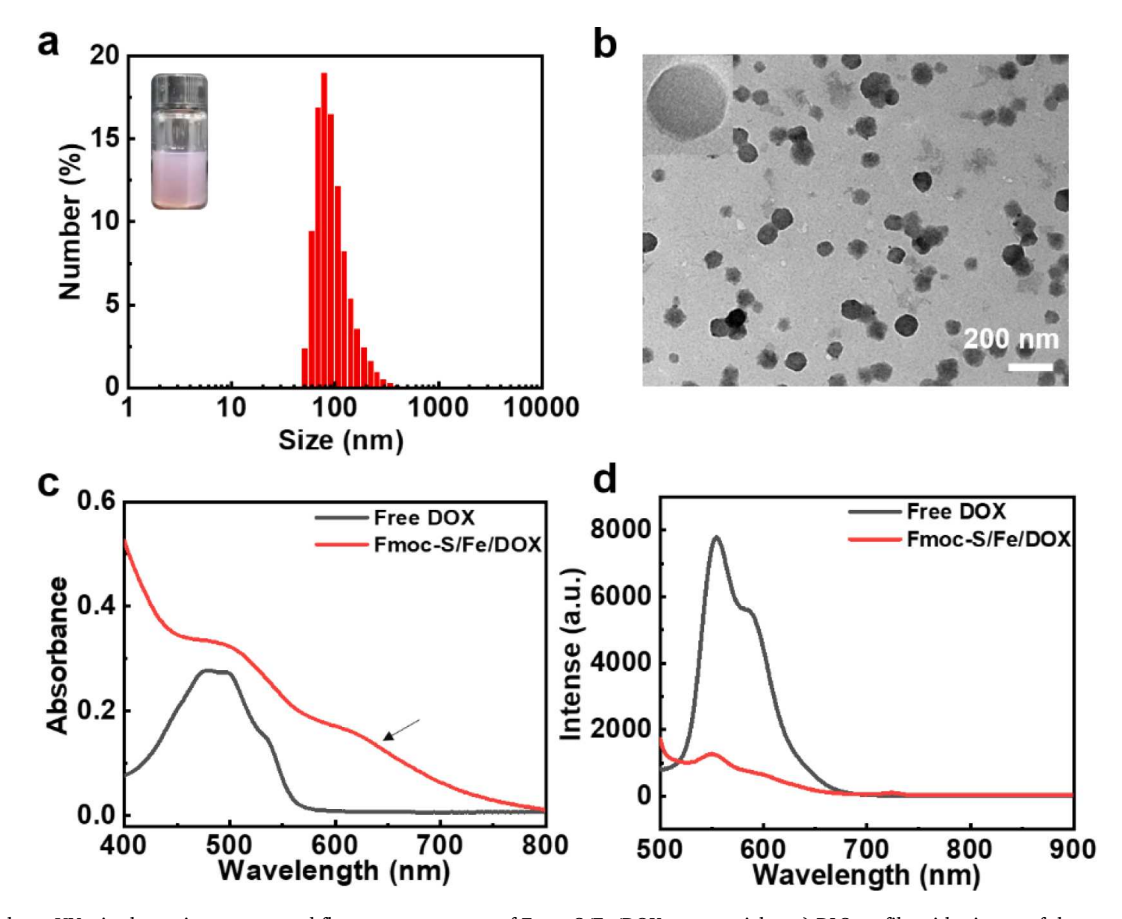


Fig. 3. Morphology, UV-vis absorption spectra and fluorescence spectra of Fmoc-S/Fe/DOX nanoparticles. a) DLS profile with picture of the sample shown in the inset. b) TEM image. c) UV-vis absorption spectra. d) Fluorescence spectra.

containing Fmoc-Cys clusters and solidified shell of Fmoc-Cys/Fe complexes sequentially, in constrast, the formation of supramolecular Fmoc-S/Fe soild nanoparticles, as Fig. 2e showed, which was resulted from the formation of preliminary ferric coordination complex and further organization of the resulting complexes based on multiple other weak interaction, including hydrophobic interaction, intermolecular hydrogen bonds and π - π stacking, the existence of which has been confirmed by the simulation results (Figure S2 and S3).

Encouraged by the robust coordination self-assembly between Fmoc-S and Fe³⁺, we investigated the feasibility of construction of multicomponent assemblies based on the co-coordination interaction among Fmoc-S, Fe³⁺, and DOX. DOX was chosen as the model building block owing to the integration of in these advantages of a typical clinical chemotherapeutic drug and the metal-binding group, i.e., amidogen and hydroxyl. After mixing of DOX and FeCl₃ in distilled water, followed by the addition of Fmoc-S, the light-red colored colloidal suspensions for Fmoc-S/Fe/DOX with the size of about 100 nm were generated (Fig. 3a). The SEM image (Figure S4) and TEM image (Fig. 3b) showed that Fmoc-S/Fe/DOX are still spherical, solid nanoparticles, and their size distributions and morphologies show no significant changes compared to that of Fmoc-S/Fe nanoparticles. The ξ potential of Fmoc-S/Fe/DOX nanoparticles was tested to be 13.3 mV, which significantly increased than Fmoc-S/Fe nanoparticles for -3.5 mV, the reversal of surface charge indicated the involvement of DOX in Fmoc-S/Fe/DOX nanoparticles since DOX contained positively charged free amino. From UV-vis spectra, the absorption band of DOX exhibited slightly red-shifted and typical absorbance shoulder peaks between 600 and 650 nm appeared for Fmoc-S/Fe/DOX (Fig. 3c), which substantially demonstrated the coordination interaction between Fe^{3+} and DOX [21]. The fluorescence of Fmoc-S/Fe/DOX nanoparticles was dramatically suppressed compared to monomeric DOX (Fig. 3d), which attributed to the formation of non-emissive ground-state complexes [22]. The coordination interaction between amino or hydroxyl group of DOX and Fe3+ was further confirmed by IR spectra (Figure S5). Significantly, the DOX incorporation efficiency in Fmoc-S/Fe³⁺/DOX exceed 70%, such encapsulation efficiency was relatively high in terms of hydrophilic drugs [23]. And a decreased ratio of Fmoc-S was detected in the nanoparticles after addition of DOX (Table S1), because DOX occupied the coordination interaction sites of Fe ion centers. Overall, these results suggested that the cooperative coordination of DOX and Fmoc-S occurred indeed in the formation of Fmoc-S/Fe/DOX nanoparticles.

After the successful preparation of Fmoc-S/Fe/DOX nanoparticles, the catalytic mechanism of the nanoparticles as peroxidase mimics was then investigated. Considering the valence shift in catalytic process of natural peroxidase as well as high oxidation-reduction level in tumor cells, the valence state of Fmoc-S/Fe/DOX nanoparticles after mixed with high concentration of GSH was detected using ophenanthroline, which can react with Fe²⁺ to form a complex with absorbance at 512 nm. As shown in Fig. 4a, after addition of 10 mM GSH, the rapid release of Fe²⁺ was observed, and no obvious Fe²⁺ release was detected in the absence of GSH. Of note, during that reaction process, the GSH was oxidized into GSSG, which was reflected by high resolution mass spectrometry (HRMS) (Figure S6). Total conversion from GSH to GSSG after treatment of Fmoc-S/Fe nanoparticles was also observed during 24 h (Figure S7). These results confirmed the reduction of ferric ion from the + 3 to + 2 valence state by GSH in the reaction. Fe²⁺ can induce the decomposition of H₂O₂ to produce ·OH according to the Fenton-type Harber-Weiss reaction. Firstly, the change in concentraion of H₂O₂ upon mixing Fmoc-S/Fe-GSH mixture was monitored, as expected, H₂O₂ was gradually decomposed with prolonged time (Figure S8). Subsequently, we investigated the generation of ·OH when H2O2 were added to Fmoc-S/Fe-GSH mixture. The ·OH can degrade methylene blue (MB) and react with terephthalic acid (TPA) to produce 2-hydroxyterephthalic acid, which is fluorescent. As Fig. 4b showed, MB can be degraded obviously after H2O2 was added to the mixture of Fmoc-S/Fe or Fmoc-S/Fe/DOX nanoparticles with GSH. The degradation of MB by the Fmoc-S/Fe/DOX nanoparticles plus H₂O₂ or GSH was negligible. In contrast, no degradation of MB was observed merely by the Fmoc-S/ Fe/DOX nanoparticles or H₂O₂. Besides, the generated ·OH for Fmoc-S/ Fe/DOX nanoparticles could also be identified with the significant

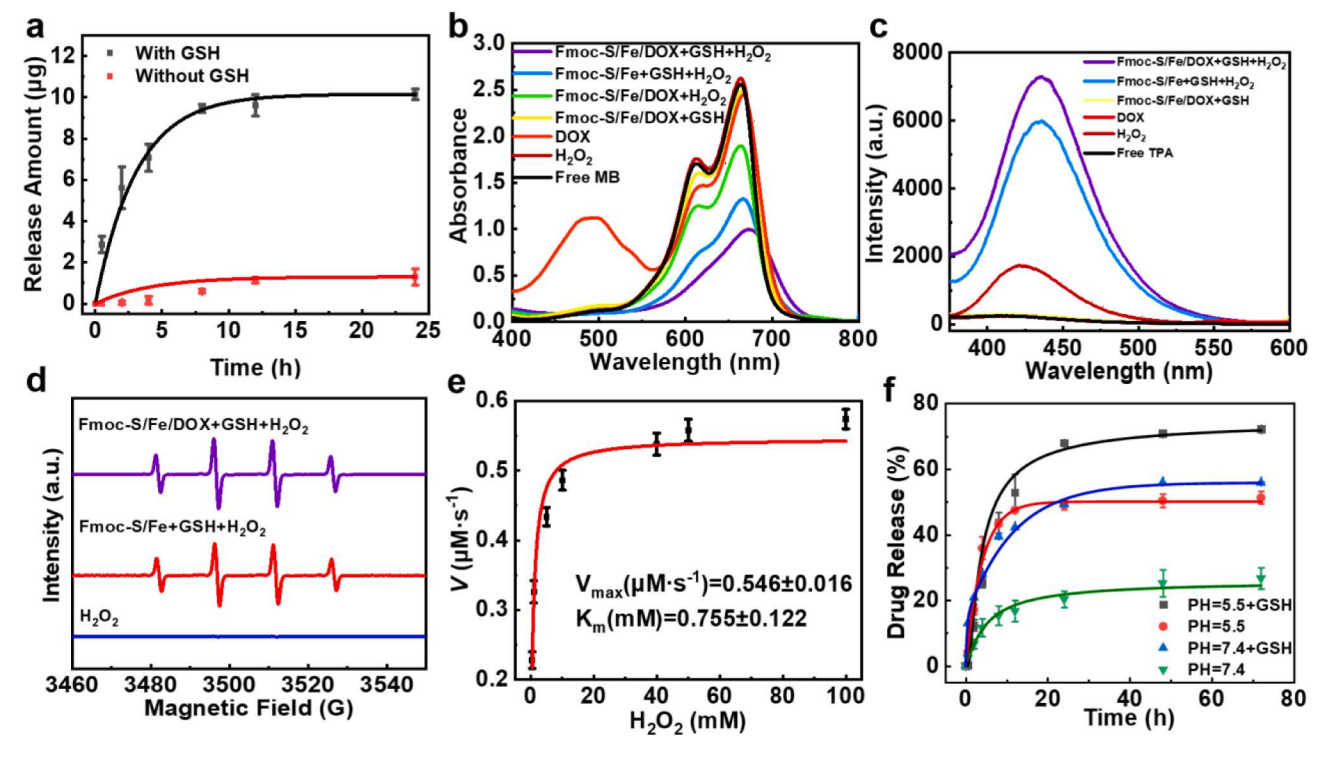


Fig. 4. The chemo-catalytic mechanism of Fmoc-S/Fe/DOX nanoparticles as peroxidase mimcs. a) GSH-triggered valence state of Fe ion from +3 to +2. b) MB degradation showing \cdot OH generation. c) The reaction of TPA with the generated \cdot OH for inducing enhancement of fluorescence. d) ESR spectra of different groups for the detection of \cdot OH. e) Kinetics for peroxidase-mimicking activity. f) pH and GSH-responsive release of DOX from nanoparticles.

fluorescence enhancement of TPA solution, wheras the fluorescence intensities of TPA solution treated with H2O2 or Fmoc-S/Fe/DOX nanopartilees alone were relatively weak (Fig. 4c). The ·OH generation ability of Fmoc-S/Fe/DOX nanoparticles was further investigated by electron spin resonance (ESR) technique. As depicted in Fig. 4d, no ·OH signals were observed in H2O2 group. In contrast, an obvious ESR signal for ·OH was detected for Fmoc-S/Fe or Fmoc-S/Fe/DOX nanoparticles in the presence of GSH. Moreover, Fmoc-S/Fe/DOX nanoparticles also generated relatively weak spectroscopic signal, which attributed to the impulse signal from hydroxy group of Fmoc-S (Figure S9). These results indicated that the Fmoc-S/Fe/DOX nanoparticles possessed peroxidase-mimicking activity, which result from the cascade catalytic reaction of conversion of Fe³⁺ to Fe²⁺ accompanied by GSH depletion firstly and subsequent ·OH generation through Fentonlike reaction of Fe²⁺. Meanwhile, the enzyme kinetics were analyzed to evaluate peroxidase-mimic activity based on steady-state kinetics with varied H₂O₂ concentration. As Fig. 4e showed, Fmoc-S/Fe nanozyme accorded with typical Michaelis-Menten model in terms of peroxidase-mimicking catalyzation. The maximum initial velocity (Vmax) was measured to be 0.55 \pm 0.016 μ M s⁻¹, Michaelis-Menten constant (Km) was determined to be 0.76 ± 0.12 mM, suggesting the higher catalytic activity of Fmoc-S/Fe nanozyme than HRP [24].

By coupling with that peroxidase-like catalytic reaction, we investigated whether the chemical drug DOX as building block could be specifically activiated in tumor tissues. The release behaviors of DOX were assessed using a dialysis method under different pH and GSH concentration, which represented circulatory system or intratumoral region (Fig. 4f). From the profiles, the release of DOX from nanoparticles were relatively insignificant at pH 7.4 and approximately 20% of DOX was released over 72 h. We further confirmed the stability of Fmoc-S/Fe/DOX nanoparticles using DLS. It was found that the size and size distribution of the nanoparticles remained unchanged in water at 37 °C in PBS or medium with 10% FBS for 24 h, suggesting the nanoparticles were very stable in circulatory system (Figure S10). Upon addition of GSH or the pH of buffer was decreased to 5.5, the release rate of DOX was dramatically accelerated. The release efficiency reached 70% at pH

5.5 in the presence of 10 mM GSH in 48 h. The GSH responsiveness may be attributed to the structure degradation of Fmoc-S/Fe/DOX nanoparticles induced by competitive chelation of GSH for Fe³⁺, whereas the response to pH is due to the protonation of the carboxyl groups at a pH below 5.5 [12e,14]. The effects of GSH and pH on nanoparticles were further investigated using DLS and TEM. As shown in Figure S11, upon incubation with GSH (3 mM) or decreasing pH as 5.5, the sizes of Fmoc-S/Fe/DOX nanoparticles were significantly increased with time, probably due to the gradual disassembly of the nanoparticles and the formation of Fmoc-S aggregates. The TEM images also clearly revealed the spherical shape has almost vanished, accompanied by self-aggregates of Fmoc-S. Hence, the high stability in blood circulation and sensitive responsiveness to pH and GSH levels suggested that the excellent specificity of the Fmoc-S/Fe/DOX metallo-nanozyme to tumor tissues.

Encouraged by the desirable catalytic activity and smart responsiveness to tumor tissue, in vitro chemo-catalytic cytotoxicity of Fmoc-S/ Fe/DOX nanoparticles was further evaluated. The cellular uptake of Fmoc-S/Fe/DOX nanoparticles was studied firstly by confocal laser scanning microscopy (CLSM). The Fig. 5a showed that the DOX fluorescence is mainly located in the cytoplasm for 2 h and that the fluorescence signal of DOX gradually diffused into nuclei for 12 h, indicated that Fmoc-S/Fe/DOX nanoparticles could be internalized by the cells and then released DOX. Next, the peroxidase-like activity of Fmoc-S/Fe/ DOX was studied based on ROS detection using dichlorofluorescein diacetate (DCF-DA) as indicators through fluorescence microscopy images (Fig. 5b and c). Compared with the control group treated with only H₂O₂, a significant enhancement in green fluorescence was observed in fluorescence image for the cells treated with Fmoc-S/Fe/DOX nanoparticles plus H₂O₂, wheras weak fluorescence was observed in cells after treated with Fmoc-S/Fe/DOX nanoparticles only, excluding the interference from fluorescence of DOX in itself. In addition, Fmoc-S/Fe nanoparticles-treated cells in the presence of H2O2 also exhibited a strong green fluorescence signal. All above observations confirmed the generation of ROS in cells, which resulting from the peroxidase-like activity of these nanoparticles. The beneath cascade enzymatic pathway in cells of peroxidase-like nanozyme was further disclosed,

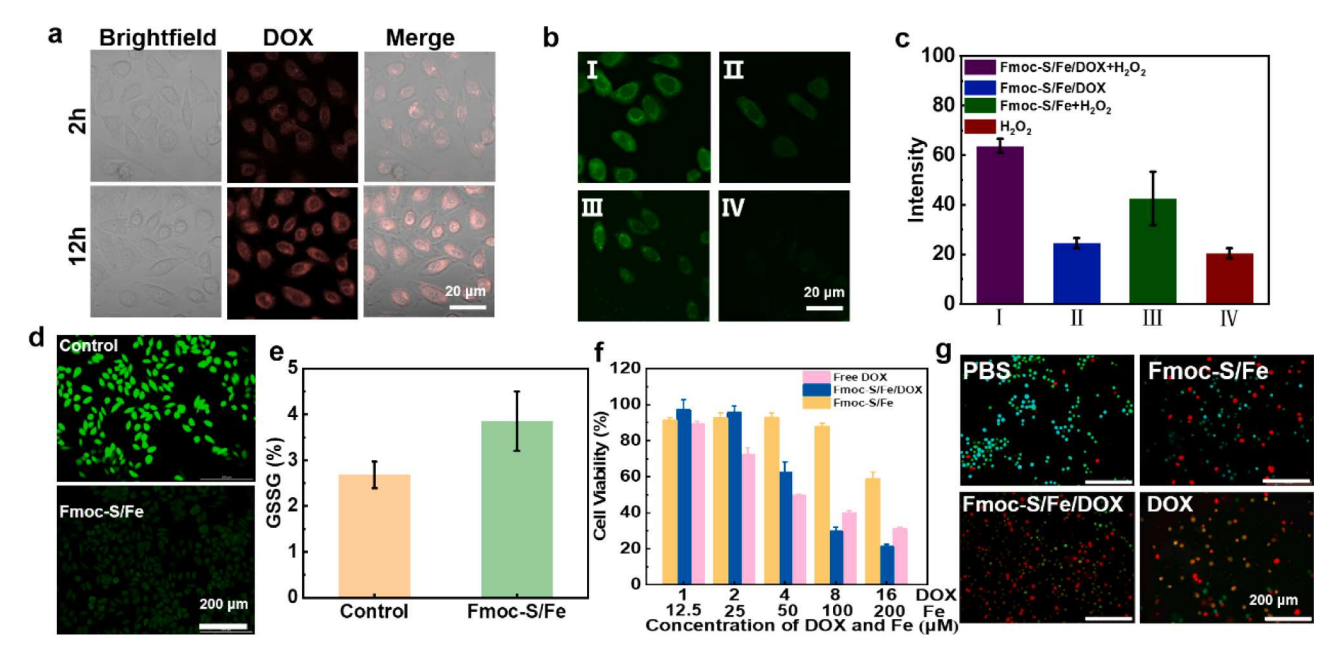


Fig. 5. Cytotoxicity of the Fmoc-S/Fe/DOX nanoparticles as metallo-nanozyme and the intracellular generation of ROS. a) CLSM image showing cellular uptake under prolonged incubation time. b) ROS staining of MCF-7 cells using DCF-DA as probe under different treatment, I: Fmoc-S/Fe/DOX nanoparticles with H_2O_2 , II: Fmoc-S/Fe/DOX nanoparticles only, III: Fmoc-S/Fe nanoparticles with H_2O_2 , IV: only H_2O_2 . c) Quantification of fluorescence intensities of DCF-DA in (b). d) Confocal images of intracellular H_2O_2 staining. e) The quantitative analysis of intracellular GSSG contents. f) MTT results of the viability of MCF-7 cells cultured with different drugs. g) Live/dead staining of MCF-7 cells, green fluorescence shows the live cells stained with calcein AM, and red fluorescence shows the dead cells stained with PI. Scale bar, 200 μm.

since Fmoc-S/Fe would greatly oxidized GSH to GSSG, the mass ratio of GSH and GSSG was studied by a GSH assay (Fig. 5e). As expected, a higher pententage of intracellular GSSG contents after treated with Fmoc-S/Fe nanoparticles was observed compared with contol group. Next, the degradation of H2O2 was studied using intracellular H2O2 assay. The MCF-7 cells treated with Fmoc-S/Fe nanoparticles exhibited barely any H2O2 fluorescence due to the peroxidase-mimicking mediated decomposition of H_2O_2 (Fig. 5d). After validating the abundant ROS generation and underlying cascade catalytic mechanism of Fmoc-S/ Fe nanoparticles in cellular level, we conducted preliminary in vitro experiments to test the cytotoxicity of the Fmoc-S/Fe/DOX nanoparticles for synergistic chemo-catalytic treatment (Fig. 5f). For a 24 h treatment with 200 µM of Fmoc-S/Fe nanoparticles and 200 µM H₂O₂, the cell viability of MCF-7 cells dropped 50%. Fmoc-S/Fe nanoparticles or H₂O₂ alone showed no cytotoxicity (Figure S12). Notably, the Fmoc-S/Fe/DOX nanoparticles-treated group exhibited stronger therapeutic efficiency as compared to that of Fmoc-S/Fe nanoparticles and free DOX nanoparticles-treated groups, indicating the elevated cooperative therapeutic effects of chemotherapy and catalytic therapy under Fmoc-S/Fe/ DOX treatment. From live/dead cell staining assay (Fig. 5g), almost no cell death was found in MCF-7 cells only treated with H₂O₂, upon the addition of Fmoc-S/Fe nanoparticles, a high cell mortality was found in MCF-7 cells, indicating the highly toxic ROS generation triggered by Fmoc-S/Fe nanoparticles. Significantly, more dead cells were observed after incubated with Fmoc-S/Fe/DOX nanoparticles, further confirming the superior effect of catalytic-chemotherapy.

Prior to testify Fmoc-S/Fe/DOX nanoparticles as potential anticancer metallo-nanozymes, the biodistribution profile in vivo was initially assessed with MCF-7 tumor cells xenograft balb/c mice. Selective tumor accumulation over time was discerned in the mice injected with the fluorochrome-labeled (FL-labeled) Fmoc-S/Fe/DOX nanoparticles, whereas the mice injected with FL showed no discernible tumor accumulation (Figure S13). Ex vivo fluorescence images also confirmed the tumor-selective distribution of the metallo-nanozyme compared to free FL(Fig. 6a, b), which may result from the EPR effect. With the excellent in vitro anticancer results and satisfactory tumor accumulation, in vivo antitumor performance of Fmoc-S/Fe/DOX nanoparticles was studied using MCF-7 tumor-bearing nude mice. Once the tumor had grown to 100 mm³, the mice were randomly divided into four groups and were injected with 5% glucose (control), free DOX, Fmoc-S/Fe/DOX nanoparticles and Fmoc-S/Fe nanoparticles, respectively. A total of 3 injections were performed over 15 days (Fig. 6c). As shown in Fig. 6d and e, the tumor size had obviously increased in the 5% glucose group, and the tumor growth had slightly inhibition in the free DOX and Fmoc-S/ Fe/DOX nanoparticles group. In contrast, there was a greatly tumor growth suppression for Fmoc-S/Fe/DOX metallo-nanozyme, indicated that the combination of chemotherapy and catalytic therapy greatly enhanced the antitumor performance. The weight and images of the tumors for each group were also determined and are showed in Fig. 6f, the tumor-inhibition rate for the mice treated with Fmoc-S/Fe/DOX nanoparticles reached 90%. As shown in the hematoxylin and eosin (H&E) staining of the tumor tissues (Fig. 6h), the mice treated with Fmoc-S/Fe/DOX nanoparticles exhibited the highest ratio of necrosis, whereas a large amount of live cancer cells were observed in the that of control group and the DOX group.

No obvious variation of body weight was detected for the therapeutic groups except that the mice treated with free DOX had a slight weight loss in the early days, which indicated the high toxicity of free DOX (Fig. 6g). Furthermore, histological analyses of the major organs including heart, liver, spleen, lung, and kidney showed that the Fmoc-S/Fe/DOX nanoparticles did not induce obvious pathological changes in these tissues (Figure S14), suggesting the negliable system toxicity of the metallo-nanozyme.

3. Conclusion

In summary, we developed a peroxidase-like metallo-nanozyme thgough multicomponent cooperative coordination self-assembly strategy based on amino acid and therapeutic drug for catalytic-chemo antitumor therpay. The obtained metallo-assemblies are well-defined spherical nanoparticles with narrow size distribution. Within tumor cells, the multicomponent nanoassemblies having peroxidasemimicking activities mediate a cascade reaction for syngestic catalytic-chemotherapy through depleting intracellular GSH and converting Fe³⁺ species to Fe²⁺ for subsequent Fenton reaction to generate abundant highly toxic ·OH for cell death, as well as the specific activation of chemical drug DOX. These features result in greatly enhanced therapeutic efficacy in vitro and in vivo, further leading to obvious tumor eradication in mice. This work not only provided a strategy for constructing biomimetic metallozyme based on small biomolecules and their cooperative coordination interation, but also offers general principles for achieving delivery and activation of metal-binding drugs for tumor-specific therapy.

4. Experimental section

4.1. Materials and methods

Fmoc-Serine (Fmoc-S), doxorubicin hydrochloride (DOX·HCl), glutathione (reduced)(GSH), terephthalic acid (TPA) and methyl thiazolyl tetrazolium (MTT) were purchased from Macklin. Iron trichloride anhydrous (FeCl₃) and Methylene blue trihydrate (MB) were obtain from Sino pharm. Transmission electron microscopy (TEM) investigations were carried out on a JSM-2100 Plus instrument. Scanning electron microscope (SEM) images were measured on Hitachi JSM-7800F. The fluorescence spectra were determined on Hitachi F-7000. The mass spectrum was determined by autoflex max MALDI-TOF in German. Dynamic light scattering (DLS) measurements were carried out on a Zetasizer Nano ZSE instrument.

4.2. Preparation of Fmoc-S/Fe nanoparticles and Fmoc-S/Fe/DOX nanoparticles

Fresh stock solution of Fmoc-S was prepared by dissolving in DMSO to give a concentration of 100 mM. Fresh stock solutions of FeCl $_3$ (10 mM) and DOX (10 mM) were prepared by dissolving in distilled water. Afterwards, a Fmoc-S stock solution (10 μ L) was added to a FeCl $_3$ stock solution (100 μ L) in distilled water (890 μ L) to obtain the Fmoc-S/Fe solution, the appearance of opalescence indicated the formation of Fmoc-S/Fe nanoparticles. The Fmoc-S/Fe/DOX nanoparticles were prepared by mixing the stock solution of Fmoc-S (10 μ L) and the stock solution of FeCl $_3$ (100 μ L) and DOX (10 μ L) with distilled water (880 μ L). The formed nanoparticles were centrifuged and washed with distilled water for three times to remove all the organic solvents and excess reactants, and then kept at room temperature.

4.3. Molecular dynamics (MD) simulations

MD simulations were performed using the program GROMACS, version 5.1.2 and an OPLS-AA force field [25]. The TIP3P model was employed to describe water molecules [26]. The force-field parameters were taken directly from the OPLS-AA force field [25]. The simulations started by minimizing the energies of the initial configuration using the steepest descent algorithm. After energy minimization, a 10 ns constant-NPT simulation (time step 1 fs) was performed to obtain a reasonable size of the solutions box. Then, a 1 ns constant-NVT simulation (time step 1 fs) was performed to pre-equilibrium the system. Finally, 50 ns constant-NVT simulations were carried out to obtain the equilibrium state. Periodic boundary conditions were employed for all xyz directions. The temperature was controlled at 298 K with Langevin

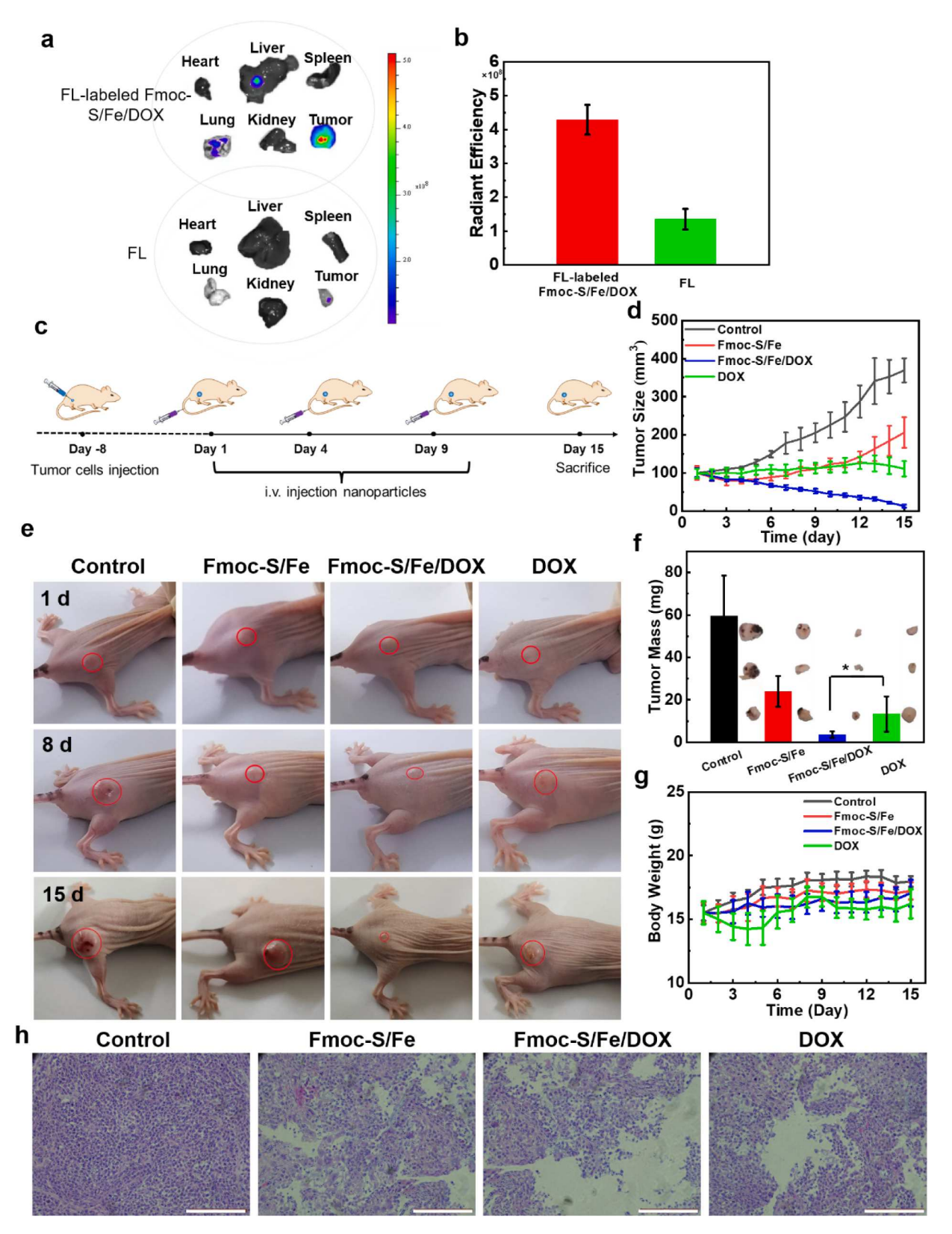


Fig. 6. In vivo antitumor studies of Fmoc-S/Fe/DOX nanoparticles compared with control groups in MCF-7 tumor-bearing mice. a) Fluorescence images of *ex vivo* mice organs and tumors harvested at 24 h post-injection. b) Quantification of fluorescence intensities of the organs and tumors in (b). c) Establishment of the subcutaneous xenografted MCF-7 cells tumor model for *in vivo* therapeutic studies. d) Tumor volumes of the tumor-bearing mice of different groups after multiple injections at the time points indicated by the red arrows. e) Photos showing the tumor size in mice during different treatment. f) The weight curves and images of tumors harvested at the end of the observation period. *p < 0.05, as calculated by the Student's *t*-test. g) Body weight of the mice in different groups. Error bars denote the standard deviation (n = 5). h) Histological analyses of the major tissues after therapy. Scale bar, 200 μm.

thermostat [27]. The pressure was kept at 1 atm using Langevin barostat [27]. The particle mesh ewald summation technique was used to calculate the long-range electrostatic interactions [28]. The nonbonded interactions were calculated based on Lennard-Jones (LJ) pair potentials which assumed the interaction occurred between two bodies [29]. LJ pair potentials were evaluated within a cut-off of 1.2 nm. The cross-interaction parameters were obtained from the Lorentz-Berthelot rules [30]. Trajectory analysis was partly done with the use of visual molecular dynamics and partly with in-house developed programs [31].

4.4. Quantitative component analysis of Fmoc-S/Fe and Fmoc-S/Fe/DOX

The solutions of Fmoc-S/Fe and Fmoc-S/Fe/DOX were centrifuged at 14000 rpm for 10 min, and the residues were re-suspended in distilled water. This process was repeated for three times to remove free ${\rm Fe}^{3+}$ not involved in the assembly. Then, the concentrations of Fmoc-S and DOX were determined by High Performance Liquid Chromatography (HPLC) (Agilent 1260 Infinity II) and UV–vis spectroscopy (Hitachi UV-2600), respectively, whereas the concentration of ${\rm Fe}^{3+}$ was measured by inductively coupled plasma-optical emission spectroscopy (ICP-OES, Perkin Elmer Avio 200).

4.5. Determination of encapsulation efficiency of DOX in the nanoparticles

The encapsulation efficiency (EE) was calculated according to the equation: EE (%) = (total drug-free drug) / total drug \times 100%. Data are expressed as EE % \pm SD of three independent experiments. The contents of DOX involved in the nanoparticles were calculated by measuring the absorbance at 480 nm of the nanoparticles in DMSO.

4.6. Investigation of stability of the nanoparticles

Fmoc-S/Fe nanoparticles and Fmoc-S/Fe/DOX nanoparticles were dispersed in PBS or in RMPI 1640 medium containing 10% FBS at 37 $^{\circ}C$ for 24 h. An aliquot of the suspensions (100 $\mu L)$ was taken out at different time intervals for DLS measurements. All measurements were performed in triplicate.

4.7. Quantitative measurement of released Fe²⁺

The release of Fe $^{2+}$ triggered by GSH was measured using a dialysis method. Specifically, Fmoc-S/Fe ([Fmoc-S] =4 mM) nanoparticles was kept inside a dialysis membrane (Mw cutoff =14000) against PBS (10 mL) in the presence of 0 or 10 mM GSH at 37 $^{\circ}\text{C}$ with constant stirring. Aliquots of each 1 mL dialysis solution was withdrawn at the selected time intervals and replaced with an equal volume of fresh medium. The released Fe $^{2+}$ in the buffer solution was collected and mixed with phenanthroline solution (100 μL , 100 mM) as Fe $^{2+}$ probe for 15 min. The phenanthroline could react with Fe $^{2+}$ to form complex with absorbance at 512 nm. The content of released Fe $^{2+}$ was determined by UV–vis absorbance at 512 nm and pre-established standard curves.

4.8. Investigation of ·OH generation of the Fmoc-S/Fe/DOX nanoparticles

Fmoc-S/Fe/DOX or Fmoc-S/Fe nanoparticles ([Fe] $=5\,$ mM) was mixed with 15 mM of GSH firstly, and then added 50 mM of $H_2O_2.$ After that, the mixtures were centrifuged at 10000 rpm for 10 min, and the supernatant was added to $10\,\mu g\,mL^{-1}$ of methylene blue (MB) solution. The generation of ·OH was as reflected by the decrease in absorbance of MB at 665 nm. For terephthalic acid (TPA) oxidation, a 5 mM TPA solution was prepared in 4 mM NaOH solution. Then, 2 mM of Fmoc-S/Fe or Fmoc-S/Fe/DOX nanoparticles were mixed with 5 mM GSH firstly, and added 10 mM of H_2O_2 to the reaction, finally the reaction product was added to the TPA. After a few minutes, the fluorescence intensity at 440 nm under excitation wavelength of 312 nm was measured.

4.9. Peroxidase-like activity of Fmoc-S/Fe/DOX nanoparticles

The kinetic assays of Fmoc-S/Fe/DOX with $\rm H_2O_2$ as a substrate were carried out. A mixed solution of Fmoc-S/Fe ([Fmoc-S] = 2 mM), TMB (0.4 mM), and $\rm H_2O_2$ at different concentrations (0.5, 1, 5, 10, 40, 50, 100 mM) was prepared. The absorbance generated from oxidized TMB at 652 nm of different reactions was monitored at different time points. The Michaelis-Menten constant (Km) and maximal velocity (Vmax) were calculated through the fitting data to Michaelis-Menten saturation curve with origin 9.0.

4.10. Responsive-Release of DOX from Fmoc-S/Fe/DOX nanoparticles

The responsive release of DOX to pH or GSH was measured using a dialysis method. Briefly, Fmoc-S/Fe/DOX nanoparticles ([DOX] $=0.6\,$ mM) was kept inside a dialysis membrane (Mw cutoff =14000) against PBS (10 mL) buffer in different pH (pH 7.4 or pH 5.5) with or without 10 mM GSH at 37 °C with constant stirring. Aliquots of each 1.0 mL dialysis solution was withdrawn at the selected time intervals and replaced with an equal volume of fresh medium. The content of released DOX was measured by UV–vis absorbance at 480 nm and pre-established standard curves of DOX.

4.11. Cell line and culture conditions

Human breast cancer cells (MCF-7) (ATCC)were maintained in RPMI-1640 medium (Procell, PM150110) supplemented with fetal bovine serum (10%) (Procell, 164210), and penicillin–streptomycin (100 units mL^{-1} and 100 $\mu g \; mL^{-1}$, respectively). The cells were grown at 37 °C in a humidified 5% CO2 atmosphere.

4.12. Cellular uptake of Fmoc-S/Fe/DOX nanoparticles

MCF-7 cells with cell density of 1×10^5 were seeded onto Petri dishes and incubated overnight at 37 °C. Then the cells were treated by Fmoc-S/Fe/DOX nanoparticles with DOX concentration of 2 μ M for 2 h and 12 h at 37 °C. After washing three times with PBS, the fluorescence was observed under 488 nm excitation using a Confocal Laser Scanning Microscopy (Axio-Imager LSM-800, German).

4.13. Intracellular ROS generation

The MCF-7 cells (1 \times 10^5 cells per well) were treated with Fmoc-S/Fe/DOX or Fmoc-S/Fe nanoparticles ([Fe] = 200 μM , [DOX] = 16 μM) in the presence and absence of H_2O_2 (200 μM) for 12 h. Then the medium was removed and the cells were further incubated with 2',7'-dichlor-odihydrofluorescein diacetate (DCF-DA, Sigma-Aldrich, 10 μM) for 30 min. DCF-DA was excited at 488 nm and its fluorescence was monitored at 493–600 nm.

4.14. Intracellular GSH depletion

The MCF-7 cells were seeded onto Petri dishes and incubated for 24 h. Then the cells were treated by Fmoc-S/Fe nanoparticles ([Fmoc-S] = $300~\mu M)$ for 12 h. The percentage of intracellular GSSG was measured using the GSH/GSSG Assay Kit (Beyotime, S0053) according to the manufacturer's instruction.

4.15. Intracellular H₂O₂ detection

The MCF-7 cells were treated with PBS and Fmoc-S/Fe nanoparticles for 12 h, the cellular $\rm H_2O_2$ level was measured by Hydrogen Peroxide Assay Kit (Abcam) according to manufacturer's instruction.

4.16. Cytotoxicity assay of Fmoc-S/Fe/DOX and Fmoc-S/Fe nanoparticles

The MTT assay was used to probe the *in vitro* cytotoxicity of these nanoparticles on MCF-7 cells. MCF-7 cells were inoculated on 96-well plates (1 \times 10 5 cells per well) for 24 h. The solutions of Fmoc-S/Fe/DOX, Fmoc-S/Fe, DOX with different concentrations were added to the 96-well plates in the presence of $\rm H_2O_2$ (200 $\mu\rm M$), respectively. After 24 h of incubation, an MTT solution in PBS (3 mg/mL, 50 $\mu\rm L$) was added to each well followed by 4 h incubation. DMSO (100 $\mu\rm L$) was then added to each well. The plate was agitated on microplate reader (HBS-1096A) for 10 s before measuring the absorbance at 490 nm for each well.

4.17. Live and dead cell staining assay

MCF-7 cells were seeded on Confocal dishes at 37 °C for 24 h. After that, previous medium was replaced by fresh medium that contained PBS, Fmoc-S/Fe nanoparticles ([Fe] = 200 μM), free DOX (16 μM), and Fmoc-S/Fe/DOX nanoparticles ([DOX] = 16 μM) in the presence of H₂O₂ (200 μM). After co-culture for 24 h, cells were stained with calcein AM (0.6 μM) and PI (1.5 μM) for 15 min and then observed using fluorescence microscopy.

4.18. In vivo biodistribution of FL-labeled Fmoc-S/Fe/DOX nanoparticles

Female balb/c nude mice with average body weight ca.16 g were bought from Beijing Weitong Lihua Experimental Animal Technical Co., Ltd. All animal experiments were conducted in accordance with the protocols approved by the local ethical committee in compliance with Chinese law for experimental animals. The mice were kept under a pathogen-free condition with free access of food and water. MCF-7 cells (5×10^7) cells in 100 µL) were inoculated subcutaneously on the back of the mice. Once the tumors were grown to the size of 200 mm³, chlorin e6 (Ce6)-loaded Fmoc-S/Fe/DOX nanoparticles and free Ce6 in 5% glucose (4 mg of Ce6 per kilogram body weight of mouse) were intravenously (i. v.) injected into the tail vein of the tumor-bearing mice. In vivo fluorescence imaging was captured before and after the injection (at different time points) with an imaging system (Perkin Elmer IVIS Lumina XRMS III, USA). At 24 h post-injection, the mice were sacrificed and different organs including liver, kidney, lung, spleen, heart and tumor were harvested for ex vivo imaging. Five mice were used for the study.

4.19. In vivo antitumor efficacy

About 100 μ L of MCF-7 cells (5 \times 10⁷ cells) were inoculated subcutaneously on the back of the mice. After the mice size reached 100 mm³, mice were divided into four groups randomly and injected with 5% glucose, Fmoc-S/Fe, Fmoc-S/Fe/DOX and free DOX (9.3 μ mol of DOX and 60 μ mol of Fe per kilogram body weight of mouse) via the tail vein, respectively. Multiple injections at day 1, 4 and 9 were applied. The body weight and tumor volume were measured immediately before injection. Tumor volume was calculated as V (mm³) = length \times width²/2, where width and length were the shortest and longest diameters of tumor, respectively. After the treatment, mice were executed and weights of all tumors were recorded. The tumor tissues and major organs of sacrificed mice were harvested and stained for histological analysis.

Declaration of Competing Interest

The authors declare that they have no known competing financial interests or personal relationships that could have appeared to influence the work reported in this paper.

Acknowledgment

S.Z. and Y.L. contributed equally to this work. This work was financially supported by the National Natural Science Foundation of China (No. 22107057), the Key Research and Development Project of Shandong Province (2019GSF109079), the National Science Foundation under grant number NSF/CHE-1834750, the Medical Science and Technology Development Plan Project of Shandong Province (202104050762), the Qingdao Key Health Discipline Development Fund, the Medical Science and Technology Development Plan Project of Qingdao City (2021-WJZD072, 2021-WJZD069), and the State Key Laboratory of Bio-Fibers and Eco-Textiles (Qingdao University).

Appendix A. Supplementary data

Supplementary data to this article can be found online at https://doi.org/10.1016/j.cej.2022.135312.

References

- [1] D.D. Luo, A.K. Carter, D. Miranda, J.F. Lovell, Adv. Sci. 4 (2017) 1600106.
- a) B. L. Tan, M. E. Norhaizan, Molecules 2019, 24, 252; b) L. Zong, G. Cheng, S. Liu,
 Z. Pi, Z., Liu, F. Song, J. Pharm. Biomed. Anal. 2019, 165, 268-275; c) Y. Hussain, L.
 Islam, H. Khan, R. Filosa, M. Aschner, S. Javed, Phytother. Res. 2021, 1-16; d) L.
 Gao, Y. Zhang, L. Zhao, W. Niu, Y. Tang, F. Gao, P. Cai, Q. Yuan, X. Wang, H. Jiang,
 X. Gao, Sci. Adv. 2020, 6, eabb1421.
- [3] a) G. C. Yu, M. M. Zhang, M. L. Saha, Z. W. Mao, J. Chen, Y. Yao, Z. J. Zhou, Y. J. Liu, C. Y. Gao, F. H. Huang, X. Y. Chen, P. J. Stang, J. Am. Chem. Soc. 2017, 139, 15940; b) L. Pan, J. Liu, J. Shi, Chem. Soc. Rev. 2018, 47, 6930-6946.
- [4] Q.H. Sun, Z.X. Zhou, N.S. Qiu, Y.Q. Shen, Adv. Mater. 29 (2017) 1606628.
- [5] M. Wen, J. Ouyang, C. Wei, H. Li, W. Chen, Y.N. Liu, Angew. Chem. Int. Ed. 58 (2019) 17425–17432
- [6] a) Q. Chen, C. Liang, X. Sun, J. Chen, Z. Yang, H. Zhao, L. Feng, Z. Liu, *Proc. Natl. Acad. Sci. USA* 2017, 114, 5343; b) H. Wang, X. Han, Z. Dong, J. Xu, J. Wang, Z. Liu, *Adv. Funct. Mater.* 2019, 29, 1902440; c) W. Ke, J. Li, F. Mohammed, Y. Wang, K. Tou, X. Liu, P. Wen, H. Kinoh, Y, Anraku, H. Chen, K, Kataoka, Z. Ge, *ACS Nano* 2019, 13, 2357-2369.
- [7] a) S. Gao, H. Lin, H. Zhang, H. Yao, Y. Chen, J. Shi, Adv. Sci. 2018, 1801733; b) D.
 Wang, H. Wu, C. Wang, L. Gu, H. Chen, D. Jana, L. Feng, J. Liu, X. Wang, P. Xu, Z.
 Guo, Q. Chen, and Y. Zhao, Angew. Chem. Int. Ed. 2021, 60, 3001-3007.
- [8] a) Z. Zhang, X. Zhang, B. Liu, J. Liu, J. Am. Chem. Soc. 2017,139, 5412-5419; b) L.
 Gao, X. Yan, Sci. China Life Sci. 2016, 59, 400-402.
- [9] Z. Wang, Y. Zhang, E. Ju, Z. Liu, F. Cao, Z. Chen, J. Ren, X. Qu, Nat. Commun. 9 (2018) 3334.
- [10] K. Fan, J. Xi, L. Fan, P. Wang, C. Zhu, Y. Tang, X. Xu, M. Liang, B. Jiang, X. Yan, L. Gao, Nat. Commun. 9 (2018) 1440.
- [11] a) P. Huang, D. Wang, Y. Su, W. Huang, Y. Zhou, D. Cui, X. Zhu, D. Yan, J. Am. Chem. Soc. 2014, 136, 11748-11756. b) Y. Liu, C. Ding, X Yan, P. Xie, B. Xu, L. Chen, Y. Liu, C. Liu, Y. Yu, Y. Lin, Chem. Eng. J. 2021, 420, 129894.
- [12] a) J. Han, Q. Zou, W. Su, X. Yan, Chem. Eng. J. 2020, 394, 124987; b) E. Song, Y. Li, L. Chen, X. Lan, C. Hou, C. Liu, Z. Liu, Nanoscale Adv. 2021, DOI: 10.1039/d1na00619c; c) J. Han, H. Gong, X. Ren, X. Yan, Nano Today 2021, 41, 101295. d)
 Y. Li, Q. Zou, C. Yuan, S. Li, R. Xing, X. Yan, Angew. Chem. Inter. Ed. 2018, 57, 17084; e) S. Li, Q. Zou, Y. Li, C. Yuan, R. Xing, X. Yan, J. Am. Chem. Soc. 2018, 140, 10794. f) B. Sun, R. Chang, S. Cao, L. Zhao, H. Yang, J. Li, X. Yan, C. M. Hest. Angew. Chem. Inter. Ed. 2020, 59, 20582-20588. g) H.An, M. Mamuti, X. Wang, H. Yao, M. Wang, L. Zhao, L. Li, Exploration 2021, 1, 20210153.
- [13] a) B. Sun, R. Chang, S. Cao, C. Yuan, L. Zhao, H. Yang, J. Li, X. Yan, C. M. Hest, Angew. Chem. Inter. Ed. 2020, 59, 20582-20588. b) J. Han, K. Liu, R. Chang, L. Zhao, X. Yan, Angew. Chem. Inter. Ed. 2019, 131, 2022-2026.
- [14] Y. Li, P. Sun, L. Zhao, X. Yan, K.P. Ng, P.C. Lo, Angew. Chem. Int. Ed. 132 (2020)
- [15] L. Zhao, R. Zheng, L. Liu, X. Chen, R. Guan, N. Yang, A. Chen, X. Yu, H. Cheng, S. Li, Biomaterials (2021), 120970.
- [16] a) C. Little, R. Olinescu, K. G. Reid, P. J. O'Brien, J. Biol. Chem. 1970, 245, 3632; b) P. G. Furtmüller, M. Zederbauer, W. Jantschko, J. Helm, M. Bogner, C. Jakopitsch, C. Obinger, Arch. Biochem. Biophys. 2006, 445, 199-213.
- [17] a) J. Liu, S. Chakraborty, P. Hosseinzadeh, Y. Yu, S. Tian, I. Petrik, A. Bhagi, Y. Lu, Chem. Rev. 2014, 114, 4366; b) P. J. Stephens, D. R. Jollie, A. Warshel, Chem. Rev. 1996, 96, 2491-2514; c) C. Zhang, C. Chen, H. Dong, J.-R. Shen, H. Dau, J. Zhao, Science 2015, 348, 690.
- [18] Q. Cui, J. Q. Wang, Y. G. Assaraf, L. Ren, P. Gupta, L. Wei, C. R. A. Jr., D. H. Yang, A. S. Chen, *Drug Resist. Updat.* 41, 2018, 1-25; b) J. Wang, Z. Yuan, *Cell Biochem Biophys.* 2013, 67, 199-206.
- [19] a) K. D. Mjos, J. F. Cawthray, G, Jamieson, J. A. Foxb, C. Orvig, *Dalton Trans.* 2015, 44, 2348; b) S. A. Boyd, L. E. Sommers, D. W. Nelson, *Soil Sci. Soc. Am. J.* 1981, 45, 1241.
- [20] P.Y. Liu, Z.H. Miao, K. Li, H. Yang, L. Zhen, C.Y. Xu, Colloids Surf. B. Biointerfaces 167 (2018) 183.

- [21] a) K. Han, W. Y. Zhang, J. Zhang, Z. Y. Ma, H. Y. Han, Adv. Healthcare Mater. 2017,
 6, 1700470; b) R. Anand, F. Borghi, F. Manoli, I. Manet, V. Agostoni, P. Reschiglian, R. Gref, S. Monti, J. Phys. Chem. B 2014, 118, 8532-8539.
- [22] L. Ruan, M. Wang, M. Zhou, H. Lu, J. Zhang, J. Gao, J. Chen, Y. Hu, A.C.S. Appl, Bio Mater. 2 (2019) 4703–4707.
- [23] K.W. Kasongo, R.H. Müller, R.B. Walker, Pharm. Dev. Technol. 17 (2012) 353.
- [24] L. Gao, J. Zhuang, L. Nie, J. Zhang, Y. Zhang, N. Gu, T. Wang, J. Feng, D. Yang, S. Perrett, X. Yan, Nat. Nanotechnol. 2 (2007) 577–583.
- B. Hess, C. Kutzner, D. Spoel, E. Lindahl, J. Chem. Theory Comput. 2008, 4 435-447.
 W. Damm, A. Frontera, J. T. Rives, W. L. Jorgensen, J. Comput. Chem. 1997, 18, 1955-1970.
- [26] W.L. Jorgensen, J. Chandrasekhar, J.D. Madura, R.W. Impey, M.L. Klein, J. Chem. Phys. 79 (1983) 926–935.
- [27] S.E. Feller, Y. Zhang, R.W. Pastor, B.R. Brooks, J. Chem. Phys. 103 (1995) 4613–4621.
- [28] T. Darden, D. York, L. Pedersen, J. Chem. Phys. 98 (1993) 10089–10092.
- [29] G.A. Cisneros, M. Karttunen, P. Ren, C. Sagui, Chem. Rev. 114 (2014) 779-814.
- [30] J.O. Hirschfelder, C.F. Curtiss, R.B. Bird, Molecular theory of gases and liquids, Wiley, New York, 1954.
- [31] W. Humphrey, A. Dalke, K. Schulten, J. Mol. Graph. 14 (1996) 33-38.